AIAA SciTech Forum
23–27 January 2023, National Harbor, MD & Online
AIAA SCITECH 2023 Forum

PREPRINT

DOI:10.2514/6.2023-0728

Bi-level Multidisciplinary Design Optimization of a Wing Considering Maneuver Load Alleviation and Flutter

Bernardo Bahia Monteiro,* Alasdair C. Gray, † Carlos E. S. Cesnik‡ and Ilya Kolmanovsky,§
University of Michigan, Ann Arbor, MI 48109

Fabio Vetrano¶
Airbus Operations S.A.S., Toulouse, France

The use of maneuver load alleviation (MLA) in an aircraft can lead to significant performance gains through a decrease in the aircraft's structural weight and synergies with the aerodynamic design. This paper presents a control agnostic approach for incorporating MLA in the multidisciplinary design optimization (MDO), based on expanding the design space with the addition of control surface deflections during a maneuver as design variables. In order to avoid adding design variables to the overall aircraft optimization problem, a bi-level optimization architecture is employed. The inner problem consists of minimizing the aggregated stresses during a maneuver, which are computed in a beam-based structural model coupled with aerodynamics based on the method of sections. The outer optimization problem is an aircraft range maximization MDO, evaluated on a shell-based structure model coupled with Reynolds-averaged Navier-Stokes aerodynamics. This problem is solved for a clamped wing model, with and without a geometrically non-linear flutter constraint. The inclusion of the flutter constraint is shown to impact the trends in the optimal design.

Nomenclature

Latin Letters

A	area enclosed by cross-section
B_δ	bound function for control deflection
c^*	$= 1 - 2c_{\text{fr}}$
c_{fr}	chord fraction
C_D	drag coefficient
C_L	lift coefficient
c_T	coefficient of thrust
$c_{l_\alpha}, c_{l_\delta}, c_{m_\delta}$	aerodynamic derivatives
D	drag
d	mass offsets
E	Young's modulus
$\mathcal{F}$	functions of interest for the MDO problem
$f(x,\theta)$	objective function
F_Z	vertical force at the wing root
G	shear modulus
g'	aeroelastic damping
$g(x,\theta)$	equality constraints function
G^a	vector of all active constraints
h	height of wingbox cross-section
$h(x,\theta)$	inequality constraints function
I	area moment of inertia
$\mathcal{I}$	inertia tensors
k	stiffness
$\text{KS}_{\text{failure}}$	aggregated failure criterion
L	lift
$\mathcal{L}$	Lagrangian

*PhD Candidate, Department of Aerospace Engineering, bbahia@umich.edu, AIAA Member.
†PhD Candidate, Department of Aerospace Engineering, alachris@umich.edu, AIAA Member.
‡Clarence L. (Kelly) Johnson Professor, Department of Aerospace Engineering, cesnik@umich.edu, AIAA Fellow.
§Professor, Department of Aerospace Engineering, ilya@umich.edu, AIAA Associate Fellow.
¶Research and Development Engineer, Loads and Aeroelastics, Flight Physics, fabio.vetrano@airbus.com.

m	concentrated masses
M_{fuel}	fuel mass
M_{init}	initial aircraft mass
M_l	lumped mass matrix
MTOW	maximum take-off weight
n	load factor
n_θ	number of parameters
n_e	number of beam elements
n_x	number of design variables
p	nodal coordinates
q_s	shear flow
$q_{s,0}$	closed section shear flow
$q_{s,b}$	basic shear flow
R	range
r	FEM residuals
S	shear force
t	thickness
u	FEM displacements
$\mathcal{U}$	set which contains the problems parameters
V	flight speed
w	width of wingbox cross-section
x	design variables
x_{geo}	geometric (planform) design variables
x_{struct}	structural design variables

Greek Letters

α	angle-of-attack
δ	control surface deflection
$\delta_{\max}$	bound on absolute value of control deflection
κ	curvature
λ	Lagrange multipliers associated to equality constraints
μ	Lagrange multipliers associated to inequality constraints
ν	Poisson's ratio
Ψ	adjoint vector
ρ	aggregation parameter
$\sigma_{\text{allowable}}$	allowable stress accounting for the safety factor
σ_Y	yield limit
σ_y	normal stress
τ	shear stresss
θ	problem parameters

Superscripts

$\hat{}$	related to beam model
$(\,)^*$	at the optimum
$(\,)^a$	related to active constraints

Subscripts

$(\,)_{\text{VM}}$	von Mises
$(\,)_A$	at the maneuver flight condition
$(\,)_C$	at the cruise flight condition
$(\,)_c$	centroid
$(\,)_D$	at the dive flight condition

I Introduction

The benefits of using maneuver load alleviation (MLA) for improving aircraft performance have been known since the late 1940's [1]. In a paper from 1971, White [2] reported that the use of MLA allowed for a 10% increase in the wingspan or a 13% increase in the payload for a large four-engine transonic transport aircraft. Several MLA controller architectures have been proposed since then, from the scheduling of open-loop deflections based on load factor used in those early studies, to model predictive controllers [3, 4]. Nevertheless, most studies involving MLA attempt to improve an existing design, instead of considering the use of MLA from the very beginning of the design process.

Recent advancements in the field of multidisciplinary design optimization (MDO) made it possible to directly size the airframe while accounting for the effects of MLA. Xu and Kroo [5] used an extension of the design space with

the deflection of control surfaces during a maneuver to allow for MLA and gust load alleviation (GLA) in their MDO problem formulation. The control surface deflections during the maneuver are included as design variables to account for MLA, while the gains of a proportional-derivative (PD) controller are included to account for GLA. Stanford [6] expanded this approach by optimizing the layout of the control surfaces for MLA and GLA of a transport aircraft and replaced the PD controller with a linear quadratic regulator (LQR), where the weighting matrices of the LQR are used as design variables. Haghighat *et al.* [7] introduced an approach where a single LQR controller was responsible for performing MLA and GLA. However, defining the architecture of the controller early in the design cycle, when the MDO process usually takes place, is not always desirable.

The process of airframe design has important differences in relation to the process of control law design. The airframe, being hardware, requires tooling and jigs to be manufactured, thus it can be very expensive to change the design after prototype production starts. The control law, on the other hand, is primarily software, so it is more amenable to changes and adjustments, with tuning happening as far in the design cycle as in flight testing. Therefore, it is desirable to get the airframe design locked in early, but the control law design can be done later in the design cycle. Nevertheless, the latter impacts the design of the former: the control law can be used to alleviate loads and allow for a lighter structure, or improve flight characteristics and therefore permit CG positions more favorable for performance. This poses a dilemma: how to assess the impact of the control system on the airframe characteristics without actually designing this control system? To solve this problem, a "controller agnostic" approach is proposed. This approach starts by assuming the existence of a well-designed controller and tries to find the limitations of its performance when combined with the airframe. The plant is then designed assuming closed-loop performance at the limits of achievable performance and the detailed control design is left to later in the design cycle. This type of approach was previously considered for gust load alleviation in [8].

This paper integrates a control agnostic MLA constraint similar to the one proposed by Xu and Kroo [5] into a mixed-complexity MDO problem. The optimization problem is a range maximization that builds on the one considered in [9], with the cruise range and cruise stresses calculated by detailed aerostructural analysis using a built-up shell finite element model (FEM) coupled to Reynolds-averaged Navier-Stokes (RANS) computer fluid dynamics (CFD). The MLA system is considered for load calculation in two corners of the V-g diagram, namely the maneuver and dive speeds (V_A, V_D), using a beam model that is obtained from a condensation of the built-up FEM. A bi-level optimization procedure is proposed to prevent the introduction of extra design variables in the outer, high-complexity, optimization problem. In this architecture, the inner optimizer uses a geometrically non-linear beam structural model [10] coupled with potential flow unsteady thin airfoil theory [11] to calculate optimal control deflections and trim condition for each static maneuver condition and returns the minimum stress level for a given maximum control deflection allocation. This formulation exploits the run-time difference between the detailed FEM coupled with RANS CFD analysis and the beam coupled with potential flow analysis, the latter being orders of magnitude faster.

To enable gradient-based optimization, the derivatives of the inner optimum solution with respect to the outer design variables are calculated analytically using the Lagrange multipliers of the optimal solution.

This paper is organized as follows. Section II presents the theoretical formulation of the proposed control-related metric, the mathematical background for obtaining gradients of the objective function of an optimization problem with respect to fixed parameters via Lagrange multipliers, and summarizes the condensation process from the built-up FEM to the beam FEM. Section IV presents the formulation of the optimization problem used to demonstrate this new capability, and Section V presents the analyses of the results of the various wing optimizations parameterized by the maximum control deflection allowable for MLA. Finally, Section VI presents the concluding remarks related to this work.

II Theoretical Formulation

II.A Static maneuver load alleviation as a suboptimization problem

The MLA metric considered here is based on the addition of control surface deflections as design variables to the calculation of the maximum stress during a maneuver, which is used to inform a failure constraint in the optimization problem. The origins of this approach can be found in the literature [5, 6].

To avoid increasing the number of design variables of the optimization problem in which the MLA analysis is going to be used, and to exploit the different computational costs of the various analyses present in the problem, a multilevel optimization approach is formulated. A sub-problem is defined to calculate both the aircraft trim and the optimal control deflections within allocation limits per control surface for reducing maneuver loads at two points in the V-g diagram,

namely maneuver and dive, with positive load factors. The output of the MLA analysis is the minimal failure metric ($\mathrm{KS}_{\mathrm{failure}}$), whose calculation is discussed in Section II.C. The derivatives of the optimal solution of the sub-problem with respect to the outer design variables are calculated by post-processing the solution, according to the derivation in Section II.B. The formulation of the inner optimization problems is given by

Maneuver (A)

$$\begin{aligned} \text{minimize} \quad & \mathrm{KS}_{\mathrm{failure}} \\ \text{with respect to} \quad & V, \delta \\ \text{subject to} \quad & F_Z = n\,\mathrm{MTOW} \\ & |\delta_i| \leq \delta_{\max},\ i = 1, \ldots, n_\delta \end{aligned}$$

Dive (D)

$$\begin{aligned} \text{minimize} \quad & \mathrm{KS}_{\mathrm{failure}} \\ \text{with respect to} \quad & \alpha, \delta \\ \text{subject to} \quad & F_Z = n\,\mathrm{MTOW} \\ & |\delta_i| \leq \delta_{\max},\ i = 1, \ldots, n_\delta \end{aligned}$$

where α is the body angle-of-attack, V is the flight speed, $\delta = [\delta_1, \ldots, \delta_{n_\delta}]^T$ is the vector of control surface deflections, $\delta_{\max}$ is the maximum deflection allocation for MLA, F_Z is the total vertical force, n is the load factor, and MTOW is the maximum weight of the aircraft. The difference between the maneuver and dive conditions resides in the selection of the trim variable: In the former, the root angle-of-attack is prescribed and the flight speed is solved for, while in the latter the flight speed is prescribed and the angle-of-attack solved for. A block diagram of the sub-problem is shown in Figure 1.

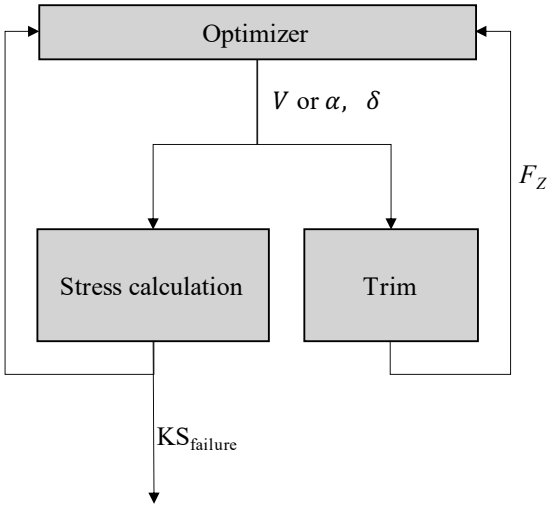

Fig. 1 Sub-optimization problem for trim and calculation of optimal MLA deflections.

II.B Sensitivity of optimal value of the objective function to the design variables

When performing gradient-based optimization in which one of the functions of interest is the output of an optimization problem, it is desirable to calculate the sensitivity of that function evaluated at the solution (*i.e.*, of the value function) with respect to the design variables of the outer problem, which are given for the inner problem. Consider the following parameter-dependent constrained optimization problem

$$\begin{aligned} \text{minimize} \quad & f(x, \theta) \\ \text{with respect to} \quad & x \\ \text{subject to} \quad & g(x, \theta) = 0 \\ & h(x, \theta) \leq 0 \end{aligned}$$

where f, g, and h are twice continuously differentiable (C^2) functions of $x \in \mathbb{R}^{n_x}$ and $\theta \in \mathcal{U} \subseteq \mathbb{R}^{n_\theta}$, where $\mathcal{U}$ is an open set. The vector θ represents the problem parameters, which correspond to the outer optimization design variables, $g(x, \theta) = 0$ are equality constraints and $h(x, \theta) \leq 0$ are inequality constraints.

Suppose, for a given value of the parameters $\theta = \theta_0$, there is a solution to this problem, denoted by $x^*(\theta_0)$ that is locally continuously differentiable in a neighborhood of θ_0 (this property holds, for instance, under strong second-order

sufficient conditions [12]). Let $\lambda^*(\theta_0)$ denote the vector of Lagrange multipliers corresponding to the equality constraints and let $\mu^*(\theta_0)$ denote the vector of Lagrange multipliers corresponding to the inequality constraints. This section summarizes the procedure to compute $\frac{\mathrm{d}f}{\mathrm{d}\theta}(x^*(\theta),\theta)\Big|_{\theta_0}$. The treatment follows [12, 13] that demonstrates that only the first-order derivative information is necessary to obtain the sensitivity of the value function, unlike the sensitivity of the solution itself that requires second-order derivatives.

Let $G^a(x,\theta)$ denote the vector function which stacks up all active constraint functions (*i.e.*, all equality constraints and active inequality constraints) of the problem and let λ^a denote the vector of corresponding Lagrange multipliers. For instance, if there are two equality constraints, $g_1(x,\theta)=0$ and $g_2(x,\theta)=0$ and two inequality constraints, $h_1(x,\theta)\leq 0$ and $h_2(x,\theta)\leq 0$, but only h_1 is active at θ_0, then $G^a=[g_1,g_2,h_1]^T$ and λ^a is the three-element vector consisting of the Lagrange multipliers corresponding to g_1, g_2, and h_1, *i.e.*, $\lambda^a=[\lambda_1,\lambda_2,\mu_1]^T$. With this notation, the Lagrangian of the problem can be written as

$$\mathcal{L}(x,\theta,\lambda^a)=f(x,\theta)+(\lambda^a)^T G^a(x,\theta). \tag{1}$$

Since the stationarity condition must hold at the minimizer, it follows that

$$\frac{\partial\mathcal{L}}{\partial x}(x^*(\theta),\theta,\lambda^{a*}(\theta))=\frac{\partial f}{\partial x}(x^*(\theta),\theta)+(\lambda^{a*}(\theta))^T\frac{\partial G^a}{\partial\theta}(x^*(\theta),\theta)=0. \tag{2}$$

Also note that the problem constraints must be satisfied for all parameters $\theta\in U$, *i.e.*,

$$G^a(x^*(\theta),\theta)=0\quad\forall\theta\in\mathcal{U}. \tag{3}$$

Then the value of the Lagrangian at the minimizer is a function only of the problem parameters and its total derivative can be calculated as

$$\begin{aligned}\frac{\mathrm{d}\mathcal{L}}{\mathrm{d}\theta}(x^*(\theta),\theta,\lambda^{a*}(\theta))=&\left[\frac{\partial f}{\partial x}(x^*(\theta),\theta)+(\lambda^{a*}(\theta))^T\frac{\partial G^a}{\partial x}(x^*(\theta),\theta)\right]\frac{\mathrm{d}x^*}{\mathrm{d}\theta}(\theta)\\&+\frac{\partial f}{\partial\theta}(x^*(\theta),\theta)+(\lambda^{a*}(\theta))^T\frac{\partial G^a}{\partial\theta}(x^*(\theta),\theta).\end{aligned} \tag{4}$$

From the stationarity condition (2), the first term is zero so it follows that

$$\frac{\mathrm{d}\mathcal{L}}{\mathrm{d}\theta}(x^*(\theta),\theta,\lambda^{a*}(\theta))=\frac{\partial\mathcal{L}}{\partial\theta}(x^*(\theta),\theta,\lambda^{a*}(\theta)). \tag{5}$$

On the other hand, (3) implies that

$$\frac{\mathrm{d}G^a}{\mathrm{d}\theta}(x^*(\theta),\theta)=\frac{\partial G^a}{\partial x}(x^*(\theta),\theta)\frac{\mathrm{d}x^*}{\mathrm{d}\theta}(\theta)+\frac{\partial G^a}{\partial\theta}(x^*(\theta),\theta)=0\quad\forall\theta\in\mathcal{U}. \tag{6}$$

Applying (6) to (4), it follows that

$$\frac{\mathrm{d}\mathcal{L}}{\mathrm{d}\theta}(x^*(\theta),\theta,\lambda^{a*}(\theta))=\frac{\partial f}{\partial x}(x^*(\theta),\theta)\frac{\mathrm{d}x^*}{\mathrm{d}\theta}(\theta)+\frac{\partial f}{\partial\theta}(x^*(\theta),\theta)=\frac{\mathrm{d}f}{\mathrm{d}\theta}(x^*(\theta),\theta). \tag{7}$$

Finally, combining results (5) and (7) and noticing that the Lagrange multipliers for inactive constraints are zero, it follows that

$$\frac{\mathrm{d}f}{\mathrm{d}\theta}(x^*(\theta),\theta)=\frac{\partial\mathcal{L}}{\partial\theta}(x^*(\theta),\theta,\lambda^*(\theta)), \tag{8}$$

which represents a simple and effective way of calculating the derivative of the optimum objective function with respect to the problem parameters using only the first derivative information. The sensitivity depends only on the knowledge of the optimum design point (x^*), Lagrange multipliers at the optimum (λ^*), and the sensitivity of the functions of interest with respect to parameters ($\frac{\partial f}{\partial\theta}$, $\frac{\partial g}{\partial\theta}$, and $\frac{\partial h}{\partial\theta}$).

For the particular case of the inner optimization problem considered here, $x=[\alpha,\delta^T]^T$, where α is the body angle of attack and δ is the vector of control deflections. From (8),

$$\frac{\mathrm{d}f}{\mathrm{d}\theta}(\alpha^*(\theta),\delta^*(\theta),\theta)=\frac{\partial f}{\partial\theta}(\alpha^*(\theta),\delta^*(\theta),\theta)+\lambda^*_\alpha\frac{\partial F_Z}{\partial\theta}(\alpha^*(\theta),\delta^*(\theta),\theta)+\lambda^*_\delta\frac{\partial B_\delta}{\partial\theta}(\delta^*(\theta)), \tag{9}$$

where $F_Z(\alpha, \delta, \theta)$ is the trim constraint and $B_\delta(\delta)$ are the bounds on control surface deflection. Since $B_\delta(\delta)$ is not a function of θ, it follows that $\frac{\partial B_\delta}{\partial \theta} = 0, \forall \theta$ and thus (9) reduces to

$$\frac{\mathrm{d}f}{\mathrm{d}\theta}(\alpha^*(\theta), \delta^*(\theta), \theta) = \frac{\partial f}{\partial \theta}(\alpha^*(\theta), \delta^*(\theta), \theta) + \lambda_\alpha^* \frac{\partial F_Z}{\partial \theta}(\alpha^*(\theta), \delta^*(\theta), \theta). \tag{10}$$

The application for the case where flight speed is used as the trim variable and the angle-of-attack is held constant is completely analogous.

II.C Stress calculation

Usually, the stress constraint used for maneuver loads in high-fidelity static aerostructural optimization is derived from the von Mises stress (or an equivalent for composite constructions) of the wingbox walls at various points along the span [14]. To obtain a similar metric from a beam based model, it is necessary to reintroduce information about the wingbox cross-section, which was lost during the condensation process. Hence, the cross section shape shown in Figure 2 is considered.

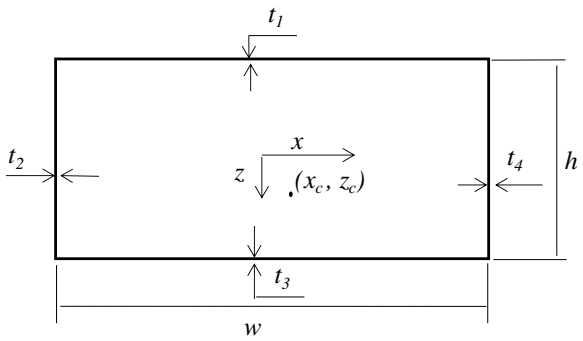

Fig. 2 Cross section models used for stress calculation. The x-axis points in the direction of flight and the z-axis points down.

The stress calculation procedure starts by computing the position of the centroid of the cross-section, which is given by

$$x_c = \frac{\frac{w}{2}(t_4 - t_2)}{w(t_1 + t_3) + h(t_2 + t_4)}, \tag{11}$$

$$z_c = \frac{\frac{h}{2}(t_3 - t_1)}{w(t_1 + t_3) + h(t_2 + t_4)}. \tag{12}$$

where the relevant dimensions and coordinate axis are shown in Figure 2.

From the Euler-Bernoulli beam formulation for isotropic material, the normal stress due to bending at a given spanwise station and at a point in the cross-section is given by

$$\sigma_y = E[\kappa_x(z - z_c) - \kappa_z(x - x_c)], \tag{13}$$

where E is the Young's modulus of the material and κ_x and κ_z are the out-of-plane and in-plane bending curvatures, respectively.

The shear stresses are calculated based on the cross-section shear flow. First, the shear flow q_s is divided into the basic shear flow $q_{s,b}$ and closed-section shear flow $q_{s,0}$, such that

$$q_s = q_{s,b} + q_{s,0}. \tag{14}$$

The basic shear flow is obtained by introducing a fictitious cut in the upper right corner of the idealized wingbox:

$$q_{s,b}(s) = \int_0^s \left(-\frac{S_x I_{xx} - S_z I_{xz}}{I_{xx} I_{zz} - I_{xz}^2} x(s) + \frac{S_z I_{zz} - S_x I_{xz}}{I_{xx} I_{zz} - I_{xz}^2} z(s) \right) t(s)\, \mathrm{d}s, \quad s \in [0, 2(w + h)], \tag{15}$$

where s is the coordinate that parameterizes the cross-section shape by arc length, S_x and S_y are the shear force resolved in the cross-sectional local coordinate frame, and I_{xx}, I_{zz}, I_{xz} are the moments of area of the cross-section. These moments are obtained by dividing the stiffness matrix of the condensed beam model (Section II.E) by the material Young's modulus and not by a direct calculation from the cross-section shape.

Finally, the closed-section shear flow is obtained by enforcing the relation between shear flow and torsion, *i.e.*,

$$\kappa_y = \frac{1}{2AG} \oint \frac{q(s)}{t(s)} \, \mathrm{d}s, \tag{16}$$

where A stands for the area enclosed by the cross-section. Applying this relation to the idealized cross-section and solving for $q_{s,0}$ yields

$$q_{s,0} = 2AG\kappa_y \frac{\oint q_{s,b}(s)/t(s) \, \mathrm{d}s}{\oint 1/t(s) \, \mathrm{d}s}. \tag{17}$$

Then the shear stresses in each skin are obtained from the shear flow by the relation

$$\tau = \frac{q_s}{t}. \tag{18}$$

Integrals (15) to (17) were solved analytically using the symbolic algebra system SymPy* and the resulting closed form solution for shear stress was sampled at the corners and the center of each wall, resulting in a total of 12 points for each cross-section. These points are chosen because they are at the extrema of the piecewise parabolic distribution of shear stress that results from this calculation. These sampled values are then combined with the normal stress from (13) using the von Mises criterion:

$$\sigma_{\mathrm{VM}} = \sqrt{\sigma_y^2 + 3\tau^2}. \tag{19}$$

The von Mises stress values are normalized by the allowable stress multiplied by a safety factor ($\sigma_{\mathrm{allowable}}$). This results in a failure metric for each point, which is aggregated using the Kreisselmeier-Steinhauser (KS) function [15–17], resulting in the final failure metric:

$$\mathrm{KS}_{\mathrm{failure}} = \frac{1}{\rho} \ln \left[\sum_{j=1}^{n_e} \sum_{i=1}^{12} \exp \left(\rho \, \frac{\sigma_{\mathrm{VM}}^{(i,j)}}{\sigma_{\mathrm{allowable}}} \right) \right], \tag{20}$$

where ρ is a parameter of the aggregation function, n_e is the number of beam elements in the structural model, index i spans the 12 points in each cross-section, and index j spans the m spanwise stations which are chosen as the edges of each beam element closest to the wing root.

The KS function is used because it is a smooth approximation of the maximum function that is also conservative and tight, *i.e.*, it approximates the maximum function from above and can get arbitrarily close to it depending on the choice of the aggregation parameter.

To summarize, the failure metric is calculated as follows: (i) The rectangular cross-section shown in Figure 2 is assumed and the normal and shear stresses of the wing at various points in the cross-section and various different spanwise stations are evaluated. (ii) These stress components are aggregated at each point using the von Mises relation, and (iii) among all points using the KS function. The inputs for the proposed stress calculation are listed in Table 1, along with the source of each piece of information in the overall MDO problem. Whenever possible, information from the beam model was used, which is obtained from the shell FEM model using a system identification procedure, described in Section II.E.

II.D Geometric parameterization

The geometric parameterization used is identical to that described in [9], *i.e.*, sweep and span are used as design variables, which are then mapped to a set of control points that define both the shell FEM and the beam nodes in a consistent way via the free-form deformation (FFD) approach. This parameterization is chosen because it keeps cross-sectional properties, such as aerodynamic chord length and jig twist angles, constant, which simplifies the model condensation process for a proof-of-concept of the methodology.

*https://www.sympy.org

Table 1 Inputs for stress calculation

Item	Symbol	Source
Material properties	E, G	Problem parameters
Cross-section shape	w, h	Problem parameters
Thicknesses	t_1, t_2, t_3, t_4	Design variables
Moments of area	I_{xx}, I_{zz}, I_{xz}	Condensed beam model
Curvatures	$\kappa_x, \kappa_y, \kappa_z$	Condensed beam model
Shear force	S_x, S_z	Condensed beam model

II.E Model condensation

The process for evaluating metrics on the condensed beam model is shown in Figure 3. It is a generalization of the method proposed in previous work [9, 18–21], which now allows for the evaluation of multiple metrics. It will be briefly summarized next.

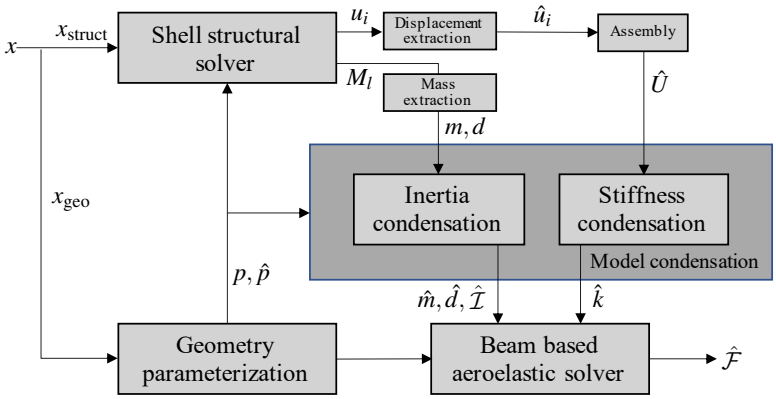

Fig. 3 Process for calculating metrics in the condensed beam model, starting from the built-up FEM

The input to the process is the vector of design variables, denoted here as x, which can be split into the structural design variables (shell element thicknesses), x_{struct}, and geometric design variables (sweep and span), x_{geo}. The latter are used to calculate the coordinates of the nodes of the built-up FEM of the wingbox, whose coordinates are denoted as p, as well as the nodes of the condensed beam model, whose coordinates are denoted as $\hat{p}$. The mass properties for the beam model are extracted from the lumped mass matrix of the built-up FEM model, M_l, and consist of concentrate masses, m, inertia tensors $\mathcal{I}$ and mass offsets, d, which are then translated to the beam reference axis and thus generate the mass properties for the beam model: $\hat{m}, \hat{\mathcal{I}}, \hat{d}$.

The stiffness properties for the beam model are calculated by an identification process based on six linear static solutions of the built-up FEM under linearly independent tip loads. The displacement of a point at the beam reference line is interpolated from each solution via RBE3 nodes and, together with the applied force values and beam node positions, used to compute the equivalent beam stiffness $\hat{k}$.

The inertia and stiffness properties $\hat{m}, \hat{\mathcal{I}}, \hat{d}, \hat{k}$, together with the node positions $\hat{p}$ fully define the aeroelastic beam model. This model can then be used to calculate functions of interest for the MDO problem, denoted here by $\hat{\mathcal{F}}$.

In the optimization presented below, three metrics are calculated using the beam model: a flutter constraint previously described in [9, 21] and two separate MLA stress constraints at the two corners of the v-g diagram corresponding to (V_A, 2.5-g) and (V_D, 2.5-g).

II.E.1 Derivatives

To calculate the derivatives of the condensed beam model metrics, denoted as $\hat{\mathcal{F}}$, with respect to the design variables x, an adjoint approach is employed:

$$\frac{\mathrm{d}\hat{\mathcal{F}}}{\mathrm{d}x} = \frac{\partial \hat{\mathcal{F}}}{\partial x} - \sum_{i=1}^{6} \psi_i^{\mathrm{T}} \left[\frac{\partial r_i}{\partial x} \right] \tag{21}$$

where r_i and u_i are the residuals and states of the ith built-up FEM structural analysis and the adjoint variables ψ_i are computed by solving:

$$\left[\frac{\partial r_i}{\partial u_i} \right]^{\mathrm{T}} \psi_i = \left[\frac{\partial \hat{\mathcal{F}}}{\partial u_i} \right]^{\mathrm{T}} \tag{22}$$

The explicit partial derivative term, $\frac{\partial \hat{\mathcal{F}}}{\partial x}$, is computed differently for the structural subset of the design variables, x_{struct}, *i.e.*,

$$\frac{\partial \hat{\mathcal{F}}}{\partial x_{\text{struct}}} = \left(\frac{\partial \hat{\mathcal{F}}}{\partial \hat{m}} \frac{\partial \hat{m}}{\partial m} + \frac{\partial \hat{\mathcal{F}}}{\partial \hat{d}} \frac{\partial \hat{d}}{\partial m} + \frac{\partial \hat{\mathcal{F}}}{\partial \hat{\mathcal{I}}} \frac{\partial \hat{\mathcal{I}}}{\partial m} \right) \frac{\partial m}{\partial M_l} \frac{\partial M_l}{\partial x_{\text{struct}}} \tag{23}$$

and for the geometric subset of the design variables, x_{geo},

$$\begin{aligned} \frac{\partial \hat{\mathcal{F}}}{\partial x_{\text{geo}}} = &\left(\frac{\partial \hat{\mathcal{F}}}{\partial \hat{p}} + \frac{\partial \hat{\mathcal{F}}}{\partial \hat{k}} \frac{\partial \hat{k}}{\partial \hat{p}} + \frac{\partial \hat{\mathcal{F}}}{\partial \hat{d}} \frac{\partial \hat{d}}{\partial \hat{p}} \right) \frac{\partial \hat{p}}{\partial x_{\text{geo}}} + \\ &+ \left[\frac{\partial \hat{\mathcal{F}}}{\partial \hat{d}} \frac{\partial \hat{d}}{\partial p} + \frac{\partial \hat{\mathcal{F}}}{\partial \hat{\mathcal{I}}} \frac{\partial \hat{\mathcal{I}}}{\partial p} + \left(\frac{\partial \hat{\mathcal{F}}}{\partial \hat{m}} \frac{\partial \hat{m}}{\partial m} + \frac{\partial \hat{\mathcal{F}}}{\partial \hat{d}} \frac{\partial \hat{d}}{\partial m} + \frac{\partial \hat{\mathcal{F}}}{\partial \hat{\mathcal{I}}} \frac{\partial \hat{\mathcal{I}}}{\partial m} \right) \frac{\partial m}{\partial p} \right] \frac{\partial p}{\partial x_{\text{geo}}} \end{aligned} \tag{24}$$

For clarity, the individual terms from these equations can be grouped by the tool used to compute them, yielding:

$$\underbrace{\frac{\partial \hat{\mathcal{F}}}{\partial \hat{p}}, \frac{\partial \hat{\mathcal{F}}}{\partial \hat{k}}, \frac{\partial \hat{\mathcal{F}}}{\partial \hat{m}}, \frac{\partial \hat{\mathcal{F}}}{\partial \hat{d}}, \frac{\partial \hat{\mathcal{F}}}{\partial \hat{\mathcal{I}}}}_{\text{Aeroelastic solver}} \quad \underbrace{\frac{\partial \hat{k}}{\partial \hat{p}}, \frac{\partial \hat{d}}{\partial \hat{p}}, \frac{\partial \hat{d}}{\partial p}, \frac{\partial \hat{\mathcal{I}}}{\partial p}, \frac{\partial \hat{m}}{\partial m}, \frac{\partial \hat{d}}{\partial m}, \frac{\partial \hat{\mathcal{I}}}{\partial m}}_{\text{Model condensation}} \quad \underbrace{\frac{\partial r_i}{\partial u_i}, \frac{\partial r_i}{\partial x}, \frac{\partial m}{\partial p}, \frac{\partial M_D}{\partial x_{\text{struct}}}}_{\text{Structural solver}} \quad \underbrace{\frac{\partial p}{\partial x_{\text{geo}}}, \frac{\partial \hat{p}}{\partial x_{\text{geo}}}}_{\text{Geometry parameterization}} \tag{25}$$

For the sake of efficiency, all the terms in the above equations not explicitly involving the output $\hat{\mathcal{F}}$ can be computed once and re-used for each component of $\hat{\mathcal{F}}$. Because the right-hand side of the adjoint system is a partial derivative of $\hat{\mathcal{F}}$, a separate set of 6 adjoint solutions are required for each output. However, since the structural solver employed uses a complete LU factorization of the stiffness matrix to solve the adjoint system, computing additional solutions with different right-hand sides can be done with a small computational cost in relation to that of the first solution.

III Computational Framework

For the computation of the range objective function and the stress constraint at cruise, the Multidisciplinary design optimization for Aircraft Configurations with High-fidelity (MACH) framework is used [14]. The structural solver used in MACH is the Toolkit for the Analysis of Composite Structures (TACS) [22], which is a shell-based FEM solver that employs an adjoint method to efficiently compute derivatives of functions of interest with respect to structural and geometric design variables. The aerodynamic solver used in MACH is ADflow [23], which is a finite-volume, cell-centered, multi-block RANS solver with the one-equation Sparlat-Almarass turbulence model. It computes the derivatives of the functions of interest with respect to aerodynamic shape variables using a discrete adjoint approach. MACH solves the coupled nonlinear aerostructural equations using the block Gauss-Seidel method with Aitken acceleration.

The beam model analysis is done by the University of Michigan's Nonlinear Aeroelastic Simulation Toolbox (UM/NAST) [10], which couples a strain-based geometrically exact beam formulation coupled with potential-flow unsteady thin airfoil theory of Peters *et al.* [11]. Compressibility effects and tip losses are accounted for using semi-empirical relations. Reverse algorithmic differentiation (RAD) is used to calculate the derivatives of the functions of interest with respect to the beam stiffness, mass properties, and position, as well as other design variables. CoDiPack [24] is used to implement RAD, and OpenMDAO [25] is used to implement the inner optimization problem.

The optimizer employed for both optimization levels is the Sparse Nonlinear OPTimizer (SNOPT) [26], which implements the gradient-based sequential quadratic programming (SQP) algorithm with a quasi-Newton approximation of the Hessian of the Lagrangian. The package pyOptSparse [27] is used to interface with SNOPT from Python.

The FFD geometry parameterization is handled by pyGeo [28], while mesh deformation due to either structural deformation or design changes is done by IDWarp [29]. The condensation from the built-up FEM model used by TACS to the beam model used by UM/NAST is handled by the University of Michigan's Enhanced FEM2Stick (UM/EF2S) [20, 30].

IV Optimization Problem Test Case

IV.A Model description

The baseline wing model used in the optimizations is shown in Figure 4 and is nearly identical to the one used in previous aerostructural optimization studies [9, 21]. The model consists of a rectangular, untwisted wing with a 1 m chord, an aspect ratio of 12, and a constant NACA 0012 aerodynamic cross-section shape. This is a stretched version of the wing used in [31].

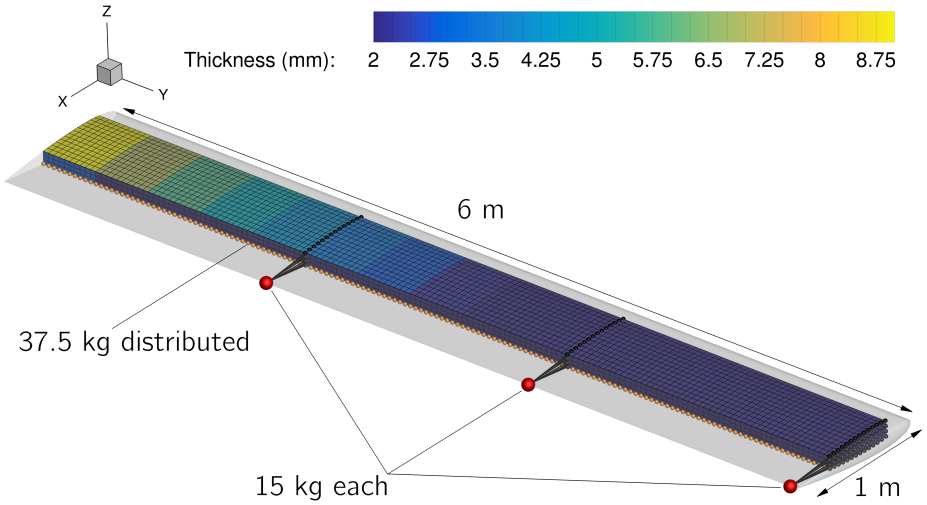

Fig. 4 Baseline wing model.

The structural wingbox spans from 15% to 65% of the aerodynamic chord and is modeled using the properties of Aluminium 2024-T3 (E = 73.1 GPa, ν = 0.33, σ_Y = 345 MPa, density = 2780 kg m^{-3}). The baseline thickness distribution (shown in Figure 4) is determined from a preliminary structural optimization under representative 2.5-g aerodynamic loads, without flutter or MLA constraints, or geometric variables. The resulting optimized structural mass is 68.5 kg. In order to ensure that this wing is flutter critical within a reasonable flight-speed range, concentrated non-structural masses were added. As done in previous work, three 15-kg non-structural point masses were added along the trailing edge at each third of the semispan. Additionally, in this work, an evenly distributed mass of 37.5 kg over the lower skin of the wingbox was added to model the effect of fuel loading. This mass is modeled both as a non-structural mass for the flutter and failure constraints evaluation and as a static inertial load in the MACH analyses used to compute quantities such as cruise drag and maneuver stresses. The wingbox mesh consists of 5,424 second-order MITC4 shell elements, giving a total of 31,296 DOF.

To evaluate the MLA-related stress constraints and the geometrically nonlinear flutter constraint, the wingbox built-up FEM is condensed to an equivalent beam model at each optimization step. The beam reference axis is at 41% of the aerodynamic chord and is discretized in 8 reference nodes, corresponding to 7 three-node beam finite elements in UM/NAST. For the stiffness condensation, each beam reference axis node is connected to the leading and trailing edges

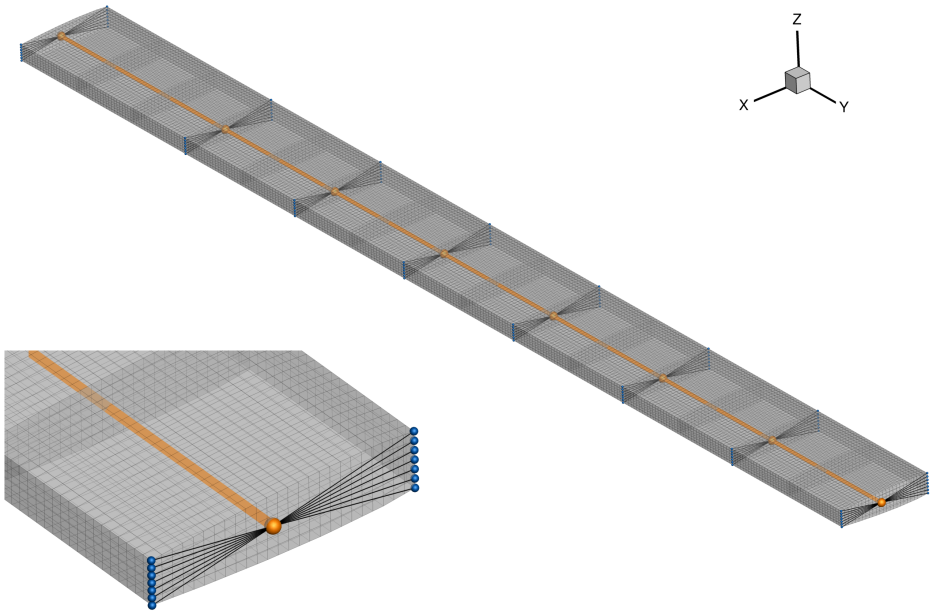

Fig. 5 Baseline wing TACS and UM/NAST structural models.

of its corresponding cross-section by TACS RBE3 element as illustrated in Figure 5. The equivalent beam model is coupled to an unsteady potential flow thin airfoil model [11].

In addition, seven control surfaces are added to the trailing edge of the UM/NAST aerodynamic model, one for each element, each spanning 15% of the chord, as shown in Figure 6. It uses linear aerodynamics with constants calculated by the same semi-empirical formulas as in [32], reproduced here:

$$c_{l_\delta} = \frac{c_{l_\alpha}}{\pi}(\cos^{-1}c^* + \sqrt{1-c^{*^2}}) \qquad c_{m_\delta} = -\frac{(1+c^*)\sqrt{1-c^{*^2}}}{2} \tag{26}$$

where $c_{l\,\alpha}$ is assumed to be $2\pi\,\mathrm{rad}^{-1}$, in line with the linearized aerodynamic model used for the NACA 0012 airfoil, and $c^* = 1 - 2c_{\mathrm{fr}}$, where c_{fr} is the length of the control surface as a fraction of the chord.

For aerostructural analyses, a structured multi-block CFD mesh is used. The surface mesh of the wing contains 22 cells along the chord, 33 along the span, and 4 across the trailing edge. This mesh is then extruded creating 40 layers that extend to a distance of 100 chord lengths from the wing. The first layer height is 5.55×10^{-6} m, which was chosen so to achieve a $y+$ value of approximately 2 at the maximum studied Reynolds number of approximately 10^7.

IV.B Optimization problem

The optimization problem considered in this work is based on [9], with the original stress at the 2.5-g load factor replaced by the MLA-related reduced order stress constraints at both the maneuvering speed, V_A, and dive speed, V_D, at 2.5-g load factor. The modified problem is shown in Table 2.

The flight conditions used in the optimization are described in Table 5. The cruise condition is used in the aerostructural analysis of the full order model and has an operating Mach number of 0.5. The cruise altitude is 10 000 m while the maneuver is performed at sea level, with flow properties being computed based on standard atmospheric values. The reduced order flutter calculations are also performed using sea-level standard atmospheric conditions, using 20 flight speeds up to $180\,\mathrm{m\,s^{-1}}$, a 15% margin on V_D. The maneuvering and dive speed conditions are used for the MLA-related reduced-order stress analyses. These analyses involve solving the sub-optimization problems shown in Tables 3 and 4.

The sub-optimization problems are used to both calculate the trim condition at V_D and V_A and the optimal static control surface deflections δ that minimize the critical stress due to bending on the wing upper and lower surfaces. A constraint on the vertical force F_Z is included to trim the wing at the 2.5-g condition. The trim is accomplished by varying the body angle of attack at a fixed speed for the dive condition and by varying the speed at a fixed body angle of

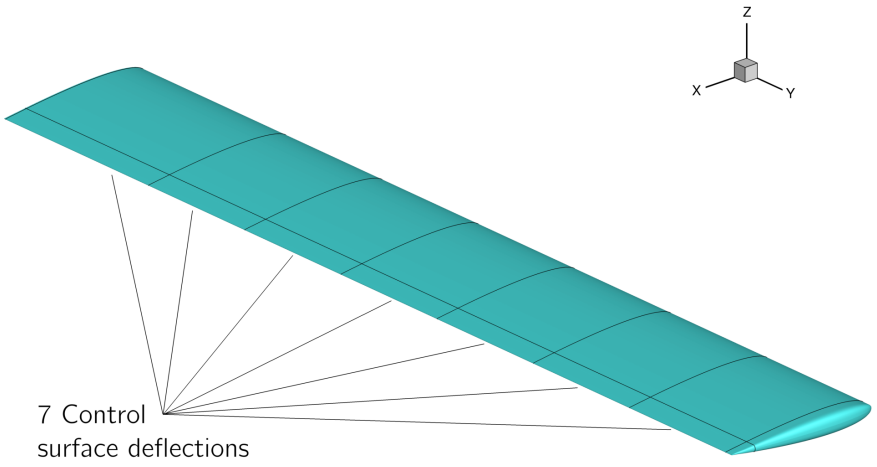

Fig. 6 Aerodynamic control surface effects included in the UM/NAST aerostructural analysis

Table 2 Outer optimization problem.

	Function/variable	Description	Quantity
maximize	R	Aircraft range	
with respect to	t	Panel thicknesses of skins/spars/ribs	28
	x_{span}	Wing semispan scaling	1
	x_{sweep}	Wing sweep	1
	α_{c}	Body angle of attack at cruise	1
		Total	**31**
subject to	$\text{KS}_{\text{flutter}} \leq 0$	KS aggregate of damping	2
	$\text{KS}_{\text{failure}}\vert_{\text{cruise}} \leq 1$	KS aggregates of 1.0 g stress values divided by allowable stress at V_C, accounting for the safety factor	4
	$\min_{\delta,\alpha_D,V_A} (\text{KS}_{\text{failure}})\vert_{\text{maneuver}} \leq 1$	KS aggregates of 2.5 g stress values divided by allowable stress at V_A and V_D, accounting for the safety factor	2
	$\lvert t_{\text{skin},\,i} - t_{\text{skin},\,i+1}\rvert \leq 1\text{mm}$	Skin adjacency constraints	12
	$\lvert t_{\text{spar},\,i} - t_{\text{spar},\,i+1}\rvert \leq 1.5\text{mm}$	Spar adjacency constraints	12
	$L = \text{MTOW}$	Trim constraint at cruise	1
		Total	**33**

Table 3 Inner optimization problem at V_D.

	Function/variable	Description	Quantity
minimize	$\text{KS}_{\text{failure}}$	KS aggregates of 2.5-g stress values divided by allowable stress multiplied by the safety factor	
with respect to	δ	Control surface deflections	7
	α_{D}	Root angle of attack at V_D	1
		Total	**8**
subject to	$F_Z = 2.5\,\text{MTOW}$	Trim constraint at constant speed	1
	$\lvert\delta_i\rvert \leq \delta_{\max}$	Bounds on control surface deflections	14
		Total	**15**

Table 4 Inner optimization problem at V_A.

	Function/variable	Description	Quantity
minimize	$\text{KS}_{\text{failure}}$	KS aggregates of 2.5-g stress values divided by allowable stress multiplied by the safety factor	
with respect to	δ	Control surface deflections	7
	V_A	Maneuvering speed	1
		Total	**8**
subject to	$F_Z = 2.5\,\text{MTOW}$	Trim constraint at constant body angle of attack	1
	$\lvert\delta_i\rvert \leq \delta_{\max}$	Bounds on control surface deflections	14
		Total	**15**

attack at the maneuvering condition, *i.e.*, V_A is effectively calculated as a by-product of the optimization. Bounds on the control surface deflections are included to limit the authority of the MLA system.

In addition to the stress constraints at the maneuvering and dive speeds, a stress constraint in the cruise condition (V_C, 1-g) is added to cover the case when the MLA system has enough authority to make the cruise condition the critical one. This constraint is calculated by the shell FEM solver and consists of the von Mises stress in the wingbox aggregated into four constraint values using KS aggregation, one each for the ribs, spars, upper skin, and lower skin panels. All stresses are constrained to lie below the material yield strength by a safety factor of safety (1.5). To produce a more realistic structural design, linear adjacency constraints are included. The thickness of adjacent panels must be within 1 mm of one another, while for the spar panels the limit is 1.5 mm.

The last constraint considered is the flutter constraint, which has been described in detail in previous work [9, 21]. It consists in linearizing the reduced order aircraft model at sampled flight conditions in the envelope (20 points are used for this example) calculating its eigenvalues and aggregating via KS functions the real part of the eigenvalues of each, which correspond to the values of modal damping at particular speeds. A second KS aggregation is used to combine the different flight conditions. The final value is then constrained to be below zero, to ensure that the aircraft is aeroelastically stable.

Figure 7 shows the structure of the OpenMDAO model used to compute the flutter and MLA stress constraints.

The objective of the outer optimization problem is to maximize range as calculated by Breguet's equation:

$$R = \frac{V_C}{c_T}\frac{C_L}{C_D}\ln\left(\frac{M_{\text{init}}}{M_{\text{init}} - M_{\text{fuel}}}\right), \tag{27}$$

where R is the flight range, V_C the cruise speed, c_T the thrust-specific fuel consumption ratio (assumed here to be $0.5\,\text{kg}\,\text{h}^{-1}$) and C_L, C_D are the cruise lift and drag coefficients, respectively, computed by the shell FEM solver coupled with RANS CFD. The initial cruise mass M_{init} consists of a fixed 400 kg plus the wingbox structural mass and the fuel mass of 37.5 kg. Note that these three masses are all half of the full aircraft values, as we only model one wing.

The design variables of the outer optimization problem are the wingbox panel thicknesses, span, sweep angle, and the body angle of attack in cruise to ensure the lift matches the load factor.

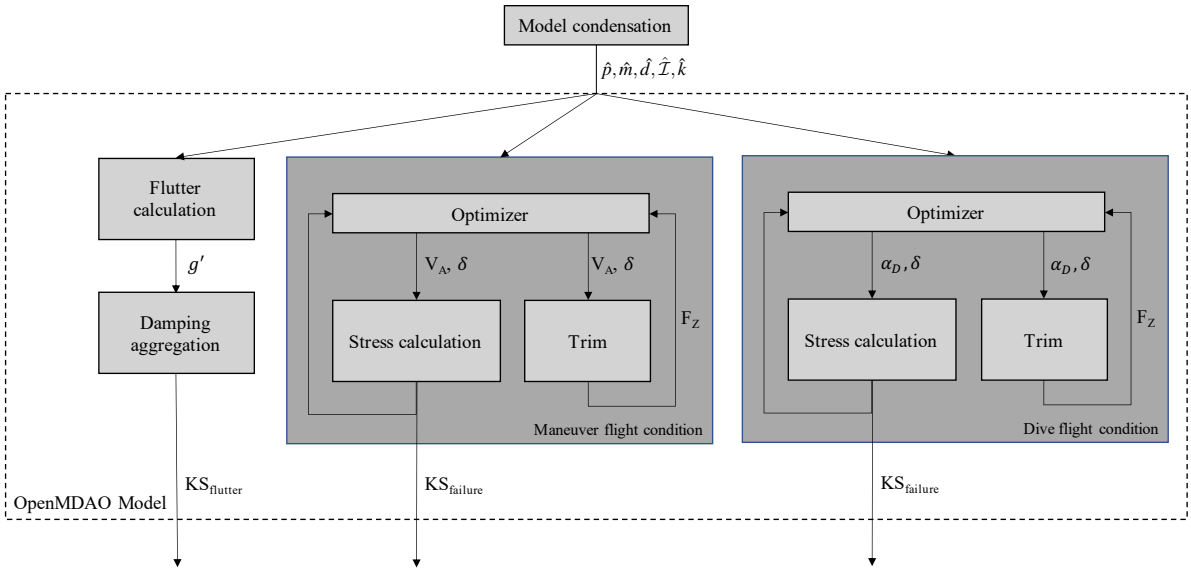

Fig. 7 Calculation of MLA constraints and geometrically nonlinear flutter constraint on the beam model

Table 5 Flight conditions used in this numerical investigation.

Condition	Speed (m/s)	Body a.o.a. (deg)	Mach	Load Factor	Altitude (m)
Cruise (C)	149.7	–	0.5	1	10000
Maneuver (A)	–	10	–	2.5	0
Dive (D)	156.5	–	0.46	2.5	0
Flutter	10–180	2	0.029–0.529	–	0

To investigate how much MLA can improve the efficiency of the wing, the optimization problem just described was solved with control surface deflection allocation limits ranging from 0 to 10°, where an allocation of 0° represents a baseline case with no MLA. These 11 optimizations were then repeated without the flutter constraint to investigate under which conditions the flutter constraint dominates the static stress constraints.

Furthermore, a constraint at V_A was included, and this constraint impacts the design even without the MLA system being active, as will be shown in the next section.

V Optimization Results

V.A Termination criteria for the inner and outer optimizer

The solver used for both the inner and outer optimization problems, SNOPT [26], implements the sequential quadratic programming (SQP) method. It divides the structure of the method into major and minor iterations, where each major iteration corresponds to a step in the nonlinear optimization problem calculated by solving a quadratic programming (QP) subproblem, which is obtained by linearizing the nonlinear problem. The minor iterations are the iterations taken to solve the QP subproblem.

To ensure the convergence of the inner optimization, which is needed for accurate calculations of the derivatives with the method described in Section II.B, the tolerances of the inner optimization were defined as follows: The "major optimality tolerance", which is imposed on the maximum norm of a scaled estimate of the gradient of the Lagrangian after each major iteration, was set to 1×10^{-10} and the "major feasibility tolerance", which is imposed on the maximum constraint violation normalized by the norm of the solution, was set to 1×10^{-6}. The maximum number of major iterations was set to 40, and the initial guess used was the solution found in the previous iteration of the outer optimizer. For a detailed description of the convergence criteria informed by these tolerances, the reader should refer to the SNOPT

manual.[†] It was checked that the inner optimizer met the convergence criteria at the last point evaluated by the outer optimizer.

The "major optimality tolerance" set for the outer optimizer was of 1×10^{-5} and the "major feasibility tolerance" was set to 1×10^{-6}. Early terminations that satisfied a "major optimality tolerance" of 1.5×10^{-3} and a "major feasibility tolerance" of 1.2×10^{-5} were considered successful.

V.B Verification of derivatives

The adjoint-based derivatives of the MLA stress constraint are verified against a finite-difference approximation. Table 6 compares the adjoint derivatives with central-difference approximations computed by perturbing the span and sweep design variables by $\pm 1 \times 10^{-4}$. The values of the stress constraint are computed with the baseline wing in the V_D condition, with a maximum control surface deflection of 3°. The largest relative difference between adjoint and finite difference values is 3.1×10^{-6}, indicating the correct implementation of the derivative chain. The derivatives with respect to the thickness design variables were also verified.

Table 6 MLA failure constraint derivatives with respect to the geometric variables $\mathbf{dKS_{failure}/dx_{geo}}$.

	$\mathbf{dKS_{failure}/dx_{Span}}$	$\mathbf{dKS_{failure}/dx_{Sweep}}$
Adjoint	**0.4150052**091137539	−0.0941349926526464
Finite-difference	**0.4150052**181406405	−0.0941352829342268
Relative error	2.2×10^{-8}	3.1×10^{-6}

V.C MLA stress constrained results

Figure 8a shows trends in a selection of values of interest across the wings optimized with differing MLA control surface allocations, represented by the maximum up or down control surface deflection, δ_{max}, and *without a flutter constraint*. In each plot, the dashed grey line denotes the value from the design optimized without MLA ($\delta_{max} = 0°$), and in the plots of the failure (MLA stress) constraints, the red line denotes the upper limit for feasibility.

In the case with the highest MLA allocation ($\delta_{max} = 10°$), the cruise range is 4.3% higher than the wing optimized without MLA. This range increase is due to a 16.6% reduction in structural mass and an increase of 1.9% in the lift-to-drag ratio (L/D). The increase in aerodynamic efficiency is attributed to an increase in span (5.7%) that outweighed the increase in sweep angle from 15° to 26°. It is worth noting that since only the span but not the chord is included as a design variable in the problem, the optimizer cannot increase the wing aspect ratio without simultaneously increasing the planform area. Furthermore, in these optimizations, the aircraft's MTOW and, therefore, the lift required in cruise were held constant, so the induced drag was not changed due to a reduction in the structural weight. The only impact of reducing the structural weight is on the initial mass M_{init} used in Breguet's range equation (27), since that is calculated by summing the structural mass with a non-structural mass with a fixed value of 400 kg and the fixed fuel mass of 37.5 kg. Therefore decreasing the structural mass increases the fraction of the total mass corresponding to fuel, which slightly increases the range of the design.

For all designs, the maneuvering speed constraint is active, while the dive speed constraint is not. Two factors contribute to this effect. Firstly, at low angles of attack (high speeds), the normal force applied to each airfoil section is larger for the same lift distribution. This causes more passive load alleviation due to the kinematic coupling caused by the back sweep, even without MLA. Secondly, the increased dynamic pressure at V_D allows the control surfaces to produce more force than at V_A, which results in more active load alleviation. This is clearly illustrated by the observation that the peak stress in the dive speed condition decreases by 49.2% across the range of control surface deflection limits, while the stress in the maneuvering speed condition remains constant at the allowed limit. The stresses at V_C rise substantially with increased control allocation for MLA, as expected, but it is worth highlighting that this can lead to fatigue issues that would require further consideration in such an MDO problem.

The optimal designs for the cases of no MLA ($\delta_{max} = 0°$) and MLA with maximum control surface allocation ($\delta_{max} = 10°$) are shown in Figure 9a. The use of MLA allows for a 2 mm reduction in skin thickness in the region close

[†]Available at https://web.stanford.edu/group/SOL/guides/sndoc7.pdf, accessed on 2 December 2022

to the wing root compared to the optimal design without MLA. There was no change in thickness at the tip, which is at the lower bound defined for this problem of 2 mm.

V.D MLA stress and flutter constrained results

Figure 8b shows the trends of the optimal wing design for varying MLA control allocations for the case *including a flutter constraint*. In this case, the flutter constraint is active for all designs and this reduces the increase in range (0.7%) enabled by the MLA system. The failure constraint at V_A is active for all designs while the one at V_D is not, for the reasons already discussed in the previous section.

The trends for changes in span and sweep with increasing control authority allocation for MLA are reversed when the flutter constraint is considered. In this case, span decreases by 4.1% and sweep decreases from 13.4° to 10.7°. This causes a reduction of 1.2% in the lift-to-drag ratio, but the loss in aerodynamic efficiency is compensated by a decrease in structural mass of 14.2%, which is comparable to the one achieved without taking flutter into account.

The observations made for the case without the flutter constraint remain valid for this case, that is, the structural mass has a small impact in the range and no fuel mass is added from the savings in structural mass. There is a substantial increase in the cruise speed stresses of 33.1%, corresponding to 67% of the allowable stress times the 1.5 safety factor.

The optimal designs for the cases of no MLA ($\delta_{\max} = 0°$) and MLA with maximum control surface allocation ($\delta_{\max} = 10°$), and the initial design (baseline) for the optimization *with* the flutter constraint are shown in Figure 9b. Comparing just the two optimized cases, the result with MLA constraints shows a reduction in panel thickness for the first half of the wing span and of up to 2.5 mm in the wingbox skins close to the root. In that same region, there is an increase in the thickness of the spars to satisfy the flutter constraint, since for this particular model the flutter is caused by the interaction between the in-plane bending and torsion modes (see [9] for a detailed discussion on the flutter mechanism).

VI Concluding Remarks

This paper proposed a bi-level multidisciplinary design optimization problem combining high and medium-complexity aeroelastic solvers, and incorporating considerations for static MLA and geometrically nonlinear flutter. The derivatives of the solution of the inner optimization problems are calculated with respect to the outer design variables using an approach based on the Lagrange multipliers, which is both efficient and accurate.

To demonstrate the proposed architecture, a series of aerostructural optimizations was performed, parameterized by the control deflection allocated for the MLA system. In these optimizations, the wing structural sizing and planform geometry were optimized to maximize cruise range, computed with a coupled RANS CFD and shell finite element model, subject to a geometrically nonlinear flutter constraint and MLA-related stress constraints at different maneuver conditions calculated using a condensed beam model coupled with 2D potential flow aerodynamics.

Without the flutter constraint, usage of MLA with up to 10° of control surface deflection allocation resulted in a 16.6% reduction in structural mass and a 4.3% increase in range. With the flutter constraint, the benefit of increasing MLA control surface allocation is reduced, with the optimal range varying by 0.7% across all studied control surface deflection limits, associated with a 14% reduction in structural mass. In both cases, the inclusion of the MLA system allows for a significant reduction in the thickness of the upper and lower surfaces of the wingbox, while the sides remain virtually unchanged for the case without the flutter constraint. When considering the flutter constraint, the side wall thicknesses close to the root are substantially increased with the inclusion of MLA, in order to prevent flutter in a more flexible wing design.

The trends for the optimal span and sweep are reversed in the cases with and without the flutter constraint when looking at the optimal values parameterized by the maximum control deflection available for MLA. Without the flutter constraint, increasing the control authority available for the MLA system causes the optimal span and sweep to increase, which results in a net increase in aerodynamic efficiency. On the other hand, for the case with the flutter constraint, the optimal values span and sweep decrease with an increase in MLA control authority. This causes the decrease in structural mass for both cases to be similar, even though the increase in range is not.

Further analysis is needed to verify whether this trend reversal can be attributed to the under-parameterization of the problem: the only design variables that modify the wing planform are span and sweep, therefore the optimizer cannot choose wing area and aspect ratio independently.

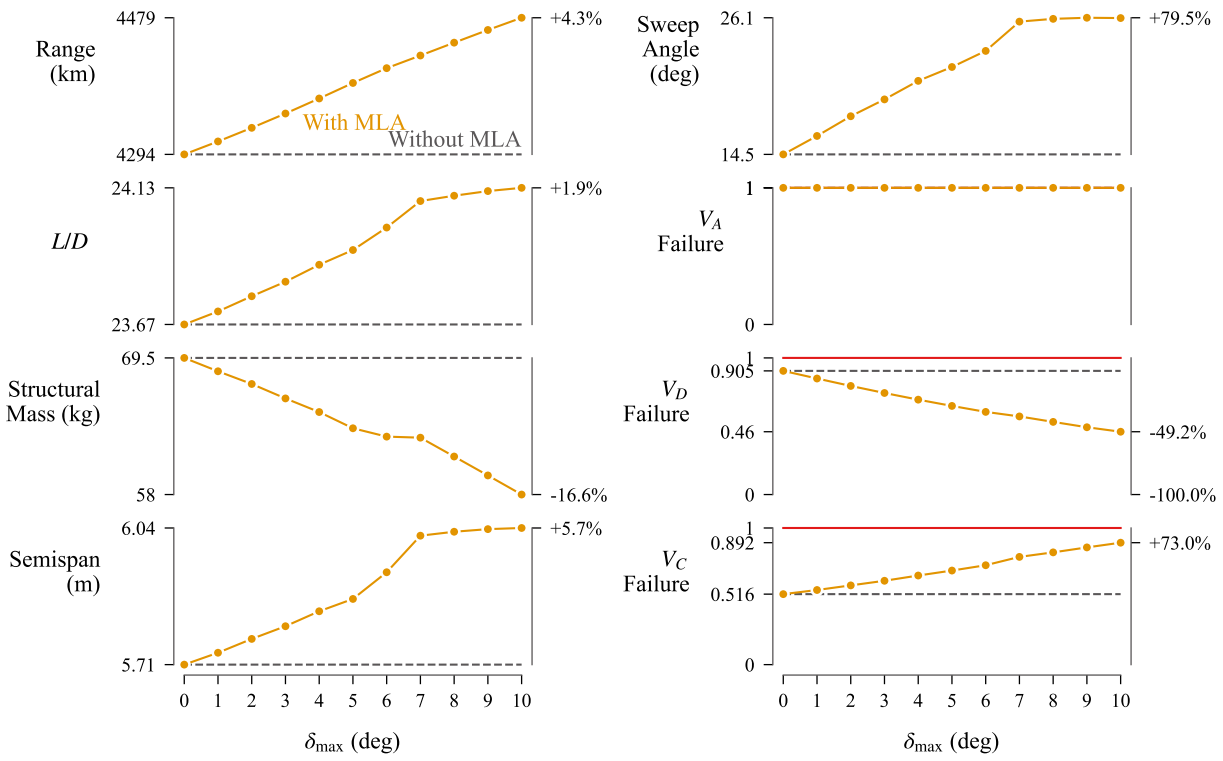

(a) without flutter constraint

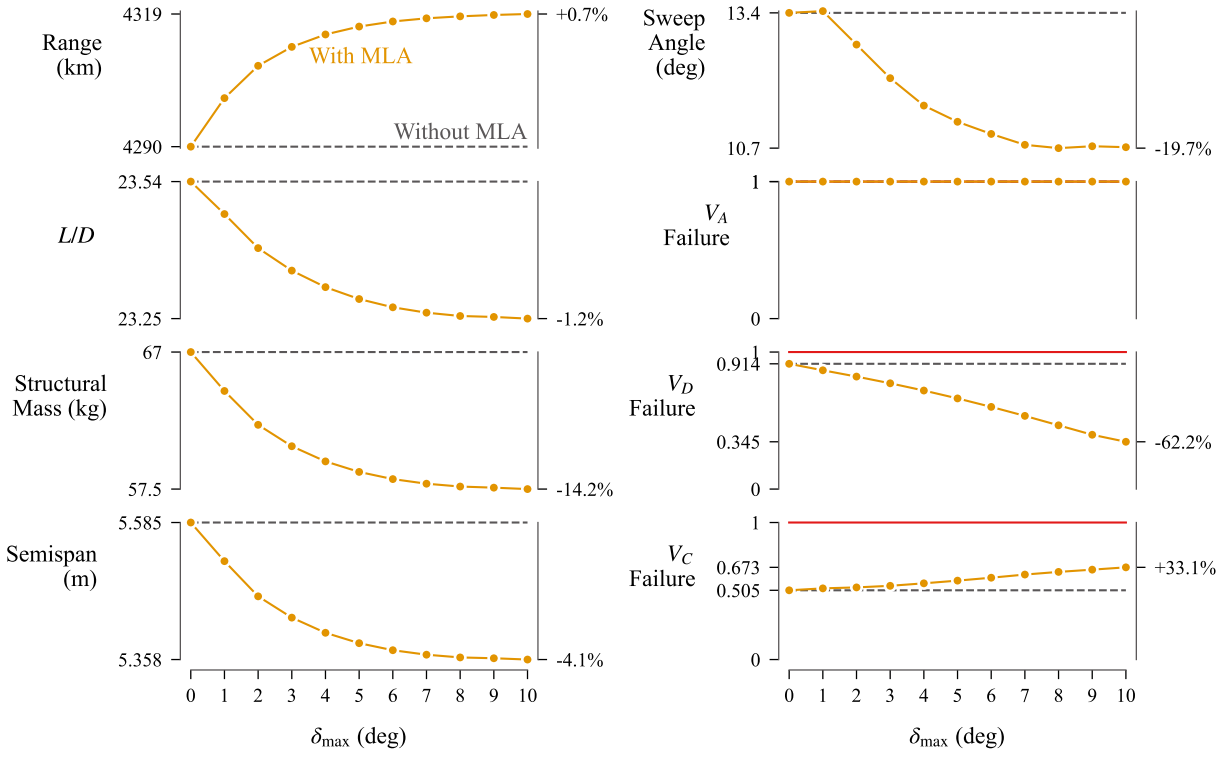

(b) with flutter constraint

Fig. 8 Selected figures of merit for the optimal designs for varying MLA control authority

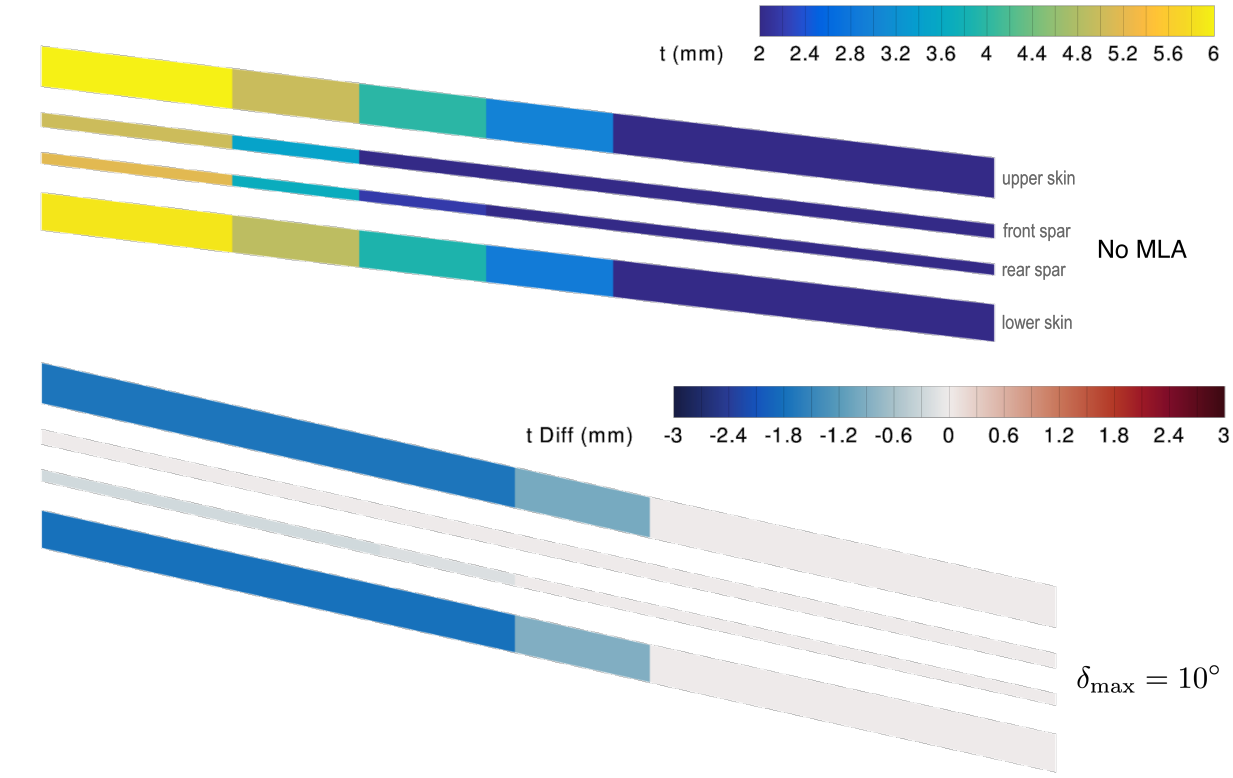

(a) without flutter constraint

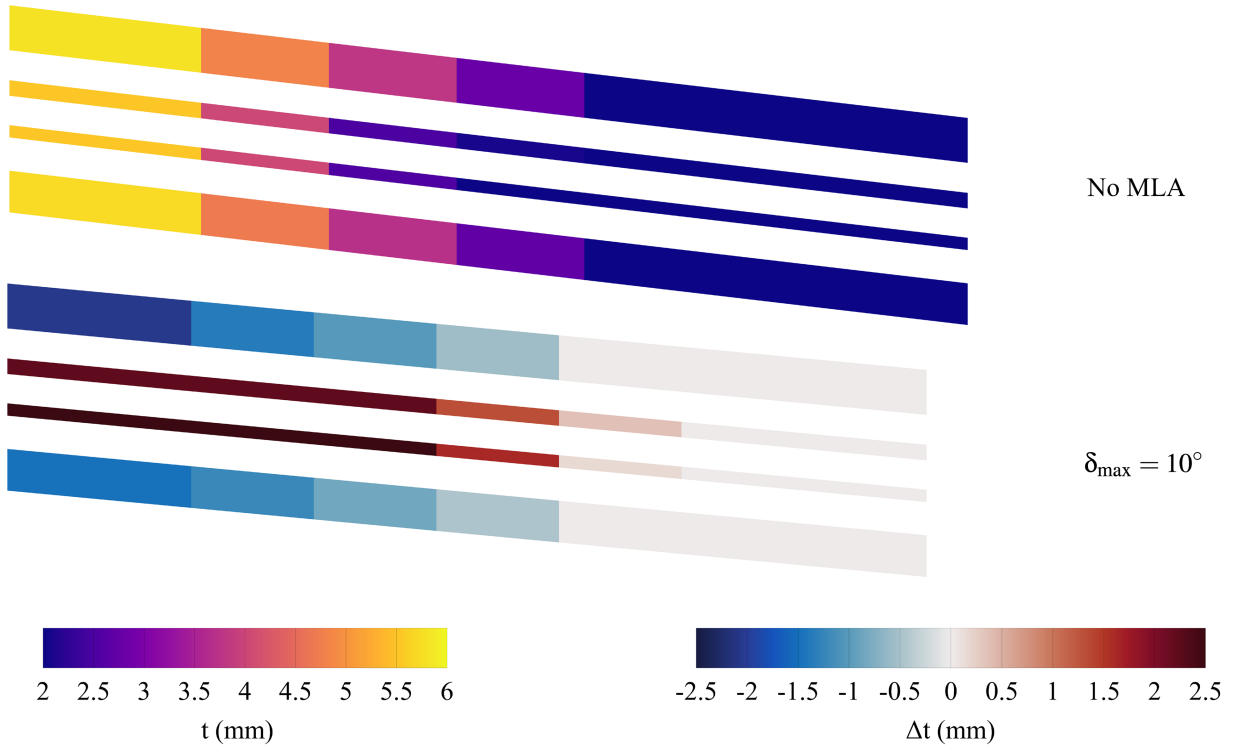

(b) with flutter constraint

Fig. 9 Optimal planform shape and thickness distribution for the cases without an MLA system and with $10°$ of MLA control authority, as a difference from the optimum without MLA.

Acknowledgments

The material of this paper is based in part upon work supported by Airbus in the frame of the Airbus-Michigan Center for Aero-Servo-Elasticity of Very Flexible Aircraft (CASE-VFA).

Bibliography

[1] Harpoothian, E., and Oswald, W. B., "Use of Ailerons to Reduce Wing Loads," , 1949. U.S. Patent 2,742,245.

[2] White, R. J., "Improving the Airplane Efficiency by Use of Wing Maneuver Load Alleviation," *Journal of Aircraft*, Vol. 8, No. 10, 1971, pp. 769–775. doi:10.2514:3.59169.

[3] Pereira, M. F. V., Kolmanovsky, I., Cesnik, C. E. S., and Vetrano, F., "Model Predictive Control Architectures for Maneuver Load Alleviation in Very Flexible Aircraft," *AIAA Scitech 2019 Forum*, 2019, p. 1591.

[4] Gaulocher, S. L., Roos, C., and Cumer, C., "Aircraft Load Alleviation During Maneuvers Using Optimal Control Surface Combinations," *Journal of Guidance, Control, and Dynamics*, Vol. 30, No. 2, 2007, pp. 591–600.

[5] Xu, J., and Kroo, I., "Aircraft Design with Active Load Alleviation and Natural Laminar Flow," *Journal of Aircraft*, Vol. 51, No. 5, 2014, pp. 1532–1545. doi:10.2514/1.c032402.

[6] Stanford, B., "Optimal Aircraft Control Surface Layouts for Maneuver and Gust Load Alleviation," *AIAA Scitech 2020 Forum*, 2020, p. 0448.

[7] Haghighat, S., Martins, J. R., and Liu, H. H., "Aeroservoelastic Design Optimization of a Flexible Wing," *Journal of Aircraft*, Vol. 49, No. 2, 2012, pp. 432–443.

[8] Bahia Monteiro, B., Cesnik, C., and Kolmanovsky, I., "Gust Load Alleviation Control Related Metric for Multidisciplinary Design Optimization," *International Forum on Aeroelasticity and Structural Dynamics*, 2022.

[9] Christison Gray, A., Riso, C., Jonsson, E., Martins, J., and Cesnik, C., "High-fidelity Aerostructural Optimization with a Geometrically Nonlinear Flutter Constraint," *International Forum on Aeroelasticity and Structural Dynamics*, 2022.

[10] Su, W., and Cesnik, C. E. S., "Nonlinear aeroelasticity of a very flexible blended-wing-body aircraft," *Journal of Aircraft*, Vol. 47, No. 5, 2010, pp. 1539–1553. doi:10.2514/1.47317.

[11] Peters, D. A., Hsieh, M. C. A., and Torrero, A., "A State-Space Airloads Theory for Flexible Airfoils," *Journal of the American Helicopter Society*, Vol. 52, No. 4, 2007, pp. 329–342. doi:10.4050/JAHS.52.329.

[12] Büskens, C., and Maurer, H., "Sensitivity analysis and real-time optimization of parametric nonlinear programming problems," *Online Optimization of Large Scale Systems*, Springer, 2001, pp. 3–16.

[13] Fiacco, A. V., *Introduction to Sensitivity and Stability Analysis in Nonlinear Programming*, Elsevier, 1983.

[14] Kenway, G. K., Kennedy, G. J., and Martins, J. R., "Scalable Parallel Approach for High-Fidelity Steady-State Aeroelastic Analysis and Adjoint Derivative Computations," *AIAA journal*, Vol. 52, No. 5, 2014, pp. 935–951.

[15] Kreisselmeier, G., and Steinhauser, R., "Systematic Control Design by Optimizing a Vector Performance Index," *International Federation of Active Controls Symposium on Computer-Aided Design of Control Systems, Zurich, Switzerland*, 1979. doi:10.1016/S1474-6670(17)65584-8.

[16] Wrenn, G. A., "An Indirect Method for Numerical Optimization Using the Kreisselmeier–Steinhauser Function," Tech. Rep. CR-4220, NASA Langley Research Center, Hampton, VA, 1989.

[17] Poon, N. M., and Martins, J. R., "An adaptive approach to constraint aggregation using adjoint sensitivity analysis," *Structural and Multidisciplinary Optimization*, Vol. 34, No. 1, 2007, pp. 61–73.

[18] Lupp, C. A., and Cesnik, C. E. S., "A Gradient-based Flutter Constraint Including Geometrically Nonlinear deformations," *AIAA Scitech 2019 Forum*, 2019. doi:10.2514/6.2019-1212.

[19] Riso, C., Sanghi, D., Cesnik, C. E., Vetrano, F., and Teufel, P., "Parametric roll maneuverability analysis of a high-aspect-ratio-wing civil transport aircraft," *AIAA Scitech 2020 Forum*, 2020, p. 1191.

[20] Riso, C., and Cesnik, C. E., "Correlations Between UM/NAST Nonlinear Aeroelastic Simulations and the Pre-Pazy Wing Experiment," *AIAA Scitech 2021 Forum*, 2021, p. 1712.

[21] Jonsson, E., Riso, C., Monteiro, B. B., Gray, A. C., Martins, J. R. R. A., and Cesnik, C. E. S., "High-Fidelity Gradient-Based Wing Structural Optimization Including a Geometrically Nonlinear Flutter Constraint," *AIAA SciTech Forum*, 2022. doi:10.2514/6.2022-2092.

[22] Kennedy, G., Kenway, G. K., and Martins, J., "High Aspect Ratio Wing Design: Optimal Aerostructural Tradeoffs for the Next Generation of Materials," *52nd Aerospace Sciences Meeting*, American Institute of Aeronautics and Astronautics, 2014. doi:10.2514/6.2014-0596.

[23] Kenway, G. K., Mader, C. A., He, P., and Martins, J. R., "Effective adjoint approaches for computational fluid dynamics," *Progress in Aerospace Sciences*, Vol. 110, 2019, p. 100542.

[24] Sagebaum, M., Albring, T., and Gauger, N. R., "High-Performance Derivative Computations using CoDiPack," *ACM Transactions on Mathematical Software (TOMS)*, Vol. 45, No. 4, 2019. doi:10.1145/3356900.

[25] Gray, J. S., Hwang, J. T., Martins, J. R. R. A., Moore, K. T., and Naylor, B. A., "OpenMDAO: An Open-Source Framework for Multidisciplinary Design, Analysis, and Optimization," *Structural and Multidisciplinary Optimization*, Vol. 59, 2019, pp. 1075–1104. doi:10.1007/s00158-019-02211-z.

[26] Gill, P. E., Murray, W., and Saunders, M. A., "SNOPT: An SQP algorithm for large-scale constrained optimization," *SIAM review*, Vol. 47, No. 1, 2005, pp. 99–131.

[27] Wu, N., Kenway, G., Mader, C. A., Jasa, J., and Martins, J. R., "pyOptSparse: A Python framework for large-scale constrained nonlinear optimization of sparse systems," *Journal of Open Source Software*, Vol. 5, No. 54, 2020, p. 2564.

[28] Kenway, G., Kennedy, G., and Martins, J. R., "A CAD-free approach to high-fidelity aerostructural optimization," *13th AIAA/ISSMO multidisciplinary analysis optimization conference*, 2010, p. 9231.

[29] Secco, N. R., Kenway, G. K., He, P., Mader, C., and Martins, J. R., "Efficient mesh generation and deformation for aerodynamic shape optimization," *AIAA Journal*, Vol. 59, No. 4, 2021, pp. 1151–1168.

[30] Riso, C., Sanghi, D., Cesnik, C. E., Vetrano, F., and Teufel, P., "Parametric Roll Maneuverability Analysis of a High-Aspect-Ratio-Wing Civil Transport Aircraft," *AIAA Scitech 2020 Forum*, American Institute of Aeronautics and Astronautics, 2020. doi:10.2514/6.2020-1191.

[31] Jonsson, E., "High-fidelity Aerostructural Optimization of Flexible Wings with Flutter Constraints," Ph.D. thesis, University of Michigan, 2020.

[32] Sanghi, D., Riso, C., Cesnik, C. E., and Vetrano, F., "Conventional and Unconventional Control Effectors for Load Alleviation in High-Aspect-Ratio-Wing Aircraft," *AIAA SCITECH 2022 Forum*, 2022, p. 4093.